

# Flow-Induced Microfluidic Assembly for Advanced Biocatalysis Materials

Phillip Lemke, Leonie Schneider, Willfried Kunz, Anna L. Rieck, Paula S. Jäger, Alexander Bruckmann, Britta Nestler, Kersten S. Rabe, and Christof M. Niemeyer\*

Exploring the potential of microfluidic systems, this study presents a groundbreaking approach harnessing energy in microfluidic flows within a purpose-built microreactor, enabling precise deposition of functional biomaterials. Upon optimizing reactor dimensions and integrating it into a microfluidic system, sequentially flow-induced deposition of DNA hydrogels and transformation into DNA-protein hybrid materials with SpyTag/SpyCatcher technology is investigated. However, limited functionalization rates restrict its viability for targeted biocatalytic processes. Therefore, the direct deposition of a phenolic acid decarboxylase is investigated, which is efficiently deposited but shows limited biocatalytic performance due to shear-induced denaturation. This challenge is overcome by a two-step immobilization process, resulting in microfluidic bioreactors demonstrating initial high space-time yields of up to  $7000 \text{ g L}^{-1} \text{ d}^{-1}$ , but whose process stability proves unsatisfactory. However, by exploiting the principle of flow-induced deposition to immobilize recombinant *E. coli* cells as functional living materials overexpressing biocatalytically relevant enzymes, bioreactors are produced that show equally high space-time yields in continuous whole-cell catalysis which remain constant over periods of up to 10 days. The insights gained offer optimization strategies for advanced functional materials and innovative reactor systems holding promise for applications in fundamental materials science, biosensing, and scalable production of microreactors for biocatalysis and bioremediation.

study of biochemical and biomedical processes, as well as countless applications in biosensing, purification, and biocatalysis.<sup>[1,2]</sup> In so-called flow biocatalysis,<sup>[3]</sup> which serves to standardize production processes and implement continuous process technology, for example, efficient immobilization methods are needed to anchor the largest possible quantities of biocatalytically active enzymes in the limited space of a microreactor. Likewise, the development of biosensing devices often requires large amounts of biomolecular sensor or transducer components to achieve maximum sensor sensitivity.<sup>[2,4]</sup> One approach to efficient immobilization of biomaterials is based on supramolecular polymerization, in which monomer units modified with recognition domains self-assemble into high-molecular-weight aggregates that are in a thermodynamic equilibrium state at the global minimum of the Gibbs free energy.<sup>[5]</sup>

More recently, increasing interest is emerging in dissipative self-assembly approaches, in which energy or mass input is dissipated to produce stable, functional assembly under nonequilibrium conditions.<sup>[6]</sup> This is a biomimetic approach

because the self-organization of biomolecules relies on a continuous flow of matter and energy for all essential life processes that control cell shape, motility, and division. To explore

## 1. Introduction

The deposition and immobilization of functional biomaterials in microfluidic systems plays a crucial role in the fundamental

P. Lemke, L. Schneider, A. L. Rieck, P. S. Jäger, A. Bruckmann, K. S. Rabe, C. M. Niemeyer  
Karlsruhe Institute of Technology (KIT)  
Institute for Biological Interfaces (IBG 1)  
Hermann-von-Helmholtz-Platz 1, D-76344 Eggenstein-Leopoldshafen,  
Germany  
E-mail: [niemeyer@kit.edu](mailto:niemeyer@kit.edu)

 The ORCID identification number(s) for the author(s) of this article can be found under <https://doi.org/10.1002/adfm.202313944>

© 2024 The Authors. Advanced Functional Materials published by Wiley-VCH GmbH. This is an open access article under the terms of the [Creative Commons Attribution-NonCommercial-NoDerivs](#) License, which permits use and distribution in any medium, provided the original work is properly cited, the use is non-commercial and no modifications or adaptations are made.

DOI: 10.1002/adfm.202313944

W. Kunz, B. Nestler  
Karlsruhe Institute of Technology (KIT)  
Institute for Applied Materials—Microstructure Modelling and Simulation  
Strasse am Forum 7, 76131 Karlsruhe, Germany  
W. Kunz, B. Nestler  
Karlsruhe University of Applied Sciences  
Institute of Digital Materials Science  
Moltkestraße 30, 76133 Karlsruhe, Germany

dissipative self-assembly of (bio)chemically synthesized components, the flow of chemical or thermal energy is typically used to induce out-of-equilibrium assembly.<sup>[7]</sup> However, the use of fluid mechanical energy has also been reported. For instance, Zheng et al. have studied the flow-driven assembly of von Willebrand factor (VWF) proteins in microfluidic structures and found that the assembly of VWF into filamentous bundles and networks is greatest in vessels with a diameter of  $\leq 300 \mu\text{m}$  that impose high shear stress and strong flow acceleration.<sup>[8]</sup> While these findings are relevant for elucidating the biophysical basis for the development and progression of microvascular diseases, materials assembly induced by micromechanical flow energy was recently exploited for the bottom-up design of dynamic biomaterials,<sup>[9]</sup> by coupling the biosynthesis of rolling circle amplification (RCA) of DNA with the shear-induced deposition occurring in microfluidic systems, equipped with designed micropillar and flow channel geometries to control the shape and mobility of the growing RCA-DNA polymer.

From a biomolecular perspective, physicochemically stable nucleic acids were hydrodynamically assembled in the latter example,<sup>[9]</sup> whereas the large multimeric glycoprotein VWF, evolved by nature for protease-mediated coagulation,<sup>[10]</sup> was used in the anterior approach.<sup>[8]</sup> To explore possible applications of this innovative concept, we wanted to investigate whether flow-induced assembly can be used to immobilize functional biomaterials that are candidates for biocatalytic applications. To this end, we report here the flow-driven assembly of nucleic acid–protein hybrid materials, active enzymes, and whole cells within microfluidic structures. Using an optimized microfluidic platform for performing and quantifying immobilization experiments, we first demonstrate that flow-induced deposition of RCA products forms DNA hydrogels that exhibit satisfactory hybridization functionality to enable the preparation of DNA–protein biohybrid materials. In contrast, deposition studies with enzymes indicate that the tertiary structure of protein molecules is denatured during immobilization, hampering the use of the immobilized enzyme materials for biocatalysis. Surprising and very significant are the results obtained with recombinant *E. coli* cells, as they were efficiently assembled into living functional biomaterials that could be used for whole-cell biocatalysis and showed very high space-time yields over long periods of time.

## 2. Results and Discussion

### 2.1. Microfluidic Platform for Flow-Induced Immobilization of Biomaterials

A general overview of the microfluidic system for flow-induced assembly of various biomaterials is shown in **Figure 1** and further details of the microfluidic setup are given in **Figure S1** (Supporting Information). To enable a wide range of deposition reactions and characterizations, the microreactor was integrated into a microfluidic system positioned inside a fluorescence microscope (**Figure S2**, Supporting Information). This allowed online observation of deposition processes using brightfield and fluorescence images, as well as automatic temperature control of the microscope chamber. The microfluidic reactor was connected to programmable syringe pumps controlled by an external script-driven control unit to enable complex experiments consist-

ing of several steps with the possibility to use different flow rates, syringe sizes, and run times followed by straightforward sampling of the reactor effluent. By using a laminar flow mixer developed by Tofteberg et al.,<sup>[11]</sup> two different solutions could be mixed for a certain predefined time before entering the reactor (**Figure S1b**, Supporting Information). The function of the mixer was previously validated for the flow rates studied ( $0.2\text{--}50 \mu\text{L min}^{-1}$ ) (**Figure S3**, Supporting Information). In addition, the integration of two microfluidic valves allowed the system to be tailored for the deposition of materials from small sample volumes, as unlimited duration of deposition and characterization processes could be realized with the help of the automatically controlled pumps. This feature, shown schematically in **Figure 1a**, was particularly useful for the initial studies on the preparation of DNA–protein biohybrid materials, for which long deposition times of up to 13 h with small amounts of sample ( $300 \mu\text{L}$ ) were used.

The microreaction cell for the flow-driven deposition of biomaterials (**Figure 1b**) contained pentagonal pillars pointing against the flow with a width of  $90 \mu\text{m}$  and the height of the entire reactor of  $20 \mu\text{m}$ , which had a spacing between the pillars of  $60 \mu\text{m}$ . The entire reactor had a length of 5 mm and a width of 1.1 mm, resulting in a total volume of 85 nL (for details on the design and specific dimensions, see **Figure S4**, Supporting Information). These dimensions result in a Reynolds number (*Re*) of 0.297 between the pillars, leading to laminar flow, assuming water as the fluid, a temperature of  $30 \text{ }^\circ\text{C}$ , and a flow rate of  $4 \mu\text{L min}^{-1}$ . Three of these deposition reactors were arranged on a microfluidic polydimethylsiloxane (PDMS) chip to allow easy parallelization of the experiments.

To evaluate whether the selected geometries, which are about six times larger than those described in the literature,<sup>[9]</sup> also generate the flow conditions required for material deposition, flow simulations of our reactor design were carried out (**Figure 1c**). The results illustrated the harsh flow conditions that occur near the pillars in the reactor. The velocity simulation revealed that the flow is alternately accelerated by the arrangement of the pillars (between the pillars) and decelerated by the widening of the channel. The narrowing of the channel at the pillars leads to strong vorticity and large shear rates, especially at the corners of the pillars. The flow simulations of the deposition reactor were performed with a high-resolution mesh using COMSOL settings: Physics-controlled mesh, element size: “Finer,”  $\approx 12.5$  million elements. Furthermore, two coarser meshes were also simulated with COMSOL using either  $\approx 1.9$  million or  $\approx 4.3$  million elements (**Figure S5**, Supporting Information). The results of the mesh analysis indicated that simulation values already converge at 12.5 million elements, so that absolute values for vorticity of about  $4200 \text{ s}^{-1}$ , shear rate of about  $4500 \text{ s}^{-1}$ , and velocity of about  $14 \text{ mm s}^{-1}$  could be estimated. A detailed description of the method can be found in the Experimental Section in the Supporting Information. Of note, the simulation results revealed that at a flow rate of  $4 \mu\text{L min}^{-1}$ , which was used for the deposition of proteins and whole cells, a high vorticity, and shear rates of up to about  $4500 \text{ s}^{-1}$  are achieved at the lateral corners of the pillars. In contrast, significantly lower shear rates of less than  $1000 \text{ s}^{-1}$  are usually achieved in conventional stirred tank reactors, depending on the process parameters.<sup>[12]</sup> The simulated flow pattern was also experimentally validated by flushing fluorescent beads through the reactor and taking fluorescence images with a high

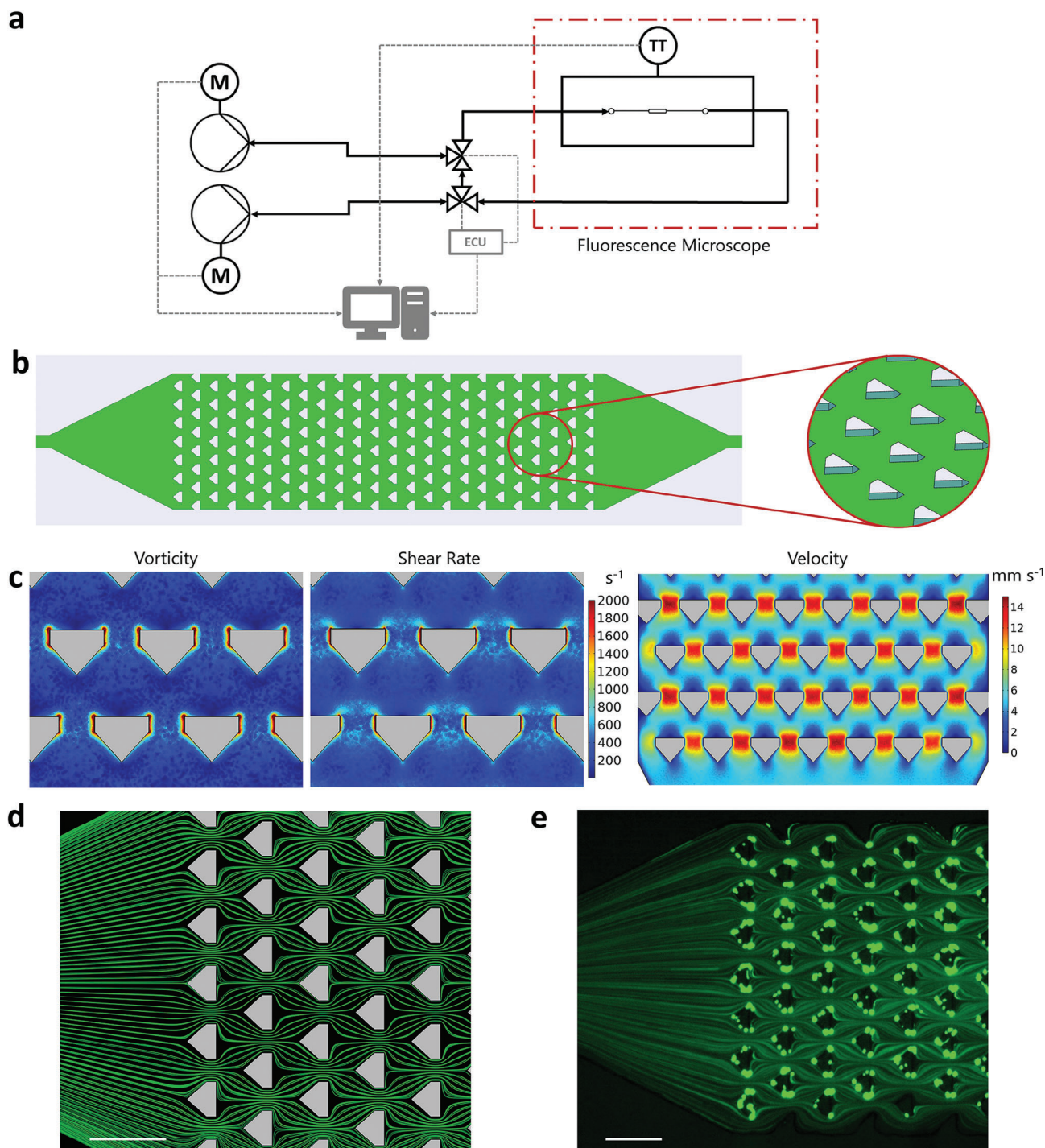


**Figure 1.** Microfluidic platform for flow-induced deposition of various biomaterials. a) Schematic overview of the microfluidic setup. The microfluidic deposition reactor is positioned inside a microscope (dash-dotted line) for online measurements of the deposition process via brightfield as well as fluorescence images. The temperature transmitter (TT) allows automatic temperature control inside the microscope. Computer-controlled motorized (M) syringe pumps enable automatic flow rate changes using a custom written script. A (semi-)continuous flow without volume restrictions can be realized with two independently controllable pumps by means of a circuit with two valves that are automatically switched by an electrical control unit (ECU). b) Schematic illustration (top view) of the microfluidic deposition reactor (left) and a close-up (oblique view) of the pillars inside the reactor (right). The 90  $\mu\text{m}$  wide pillars with a 60  $\mu\text{m}$  gap in between lead to suitable fluidic conditions for the flow-driven immobilization of biomaterials. c) Results of vorticity, shear rate, and velocity simulations. Note that the scale of vorticity and shear rate simulation results only covers the range 0–2000  $\text{s}^{-1}$  to make the smaller values visually distinguishable. This scaling results in all values  $>2000 \text{ s}^{-1}$  appearing as dark red. d) Streamline simulation. e) Experimental validation using green fluorescent beads with a diameter of 1  $\mu\text{m}$ . To visualize the streamlines, the fluorescence image was acquired with an exposure time of 250 ms. Scale bars: 200  $\mu\text{m}$ .

exposure time of 250 ms (Figure 1e). The particles adhering to the hydrophobic PDMS pillars due to adsorption were clearly visible as bright spots in these images due to their loss of mobility and in combination with the long exposure time.

## 2.2. Deposition of DNA Hydrogel Materials

Since flow-based deposition of RCA-based DNA hydrogels was performed in the work of Hamada et al. using a reactor with much smaller pillars,<sup>[9]</sup> we first wanted to test whether the deposition of DNA hydrogels could also be confirmed in the larger-scale reactor used here. Here, we aimed for a larger reaction volume, especially to simplify further process steps such as successive modification, functionalization, and characterization of the deposited material. To this end, a suitable flow rate for the deposition of the DNA materials was first determined, which was adjusted based on simulations to achieve similar vorticity and shear rates as Hamada's reactor. This resulted in a flow rate of  $1 \mu\text{L min}^{-1}$ .

To perform RCA, we used standard reagent conditions (circular template (50 nm), primer (500 nm), desoxynucleotide triphosphates (dNTPs) (50  $\mu\text{M}$ ), and phi29-polymerase (0.2  $\text{U } \mu\text{L}^{-1}$ )<sup>[13]</sup> but added 500 nm of a Cy5-fluorescently labeled nucleotide to visualize the successful formation and deposition of the DNA hydrogel. The fluorescence image acquired after 9 h showed clearly visible filamentous deposits (Figure 2a), with the fluorescence of the gel-like structures in the rear region of the reactor volume being particularly evident. In comparison, the front region of the reactor exhibited less fluorescence intensity, but magnification of this region showed that filamentous fluorescent structures were also present there. These findings suggested that the single-stranded DNA (ssDNA) formed during RCA adhered to the pillars of the reactor through the flow-induced vortices (Figure 2b), and formed an increasingly dense hydrogel material by progressive attachment and polymerization along the length of the reactor volume. The gradual accumulation of the hydrogel inside the reactor observed here has not been described before, but can be well explained by the supramolecular structure of the DNA hydrogel, which is based on the entanglement of the DNA strands. Due to the relatively large distances between the pillars, the DNA strands are presumably increasingly entangled as the length of the reactor increases, so that the DNA hydrogel can accumulate strongly, especially in the rear region of the reactor.

To evaluate the usefulness of our reactor for biocatalytic application perspectives in combination with DNA hydrogel technology, we then wanted to perform the conversion of the DNA hydrogel into a DNA-protein biohybrid material by two different modification steps under flow conditions (Figure 2b–j). For this purpose, a DNA hydrogel was first generated in the chip at a flow rate of  $1 \mu\text{L min}^{-1}$ , which could be monitored by fluorescence microscopy due to the incorporated fluorescently labeled nucleotides (Figure 2c). The material deposited in the reactor was quantified by segmentation image analysis based on the fluorescence images, as detailed in the Experimental Section and Figure S6 (Supporting Information). The time-dependent increase in covered reactor area (black) determined by image analysis showed a first significant increase already after 1.8 h (Figure 2d), whereas no comparable fluorescence increase was

observed in the corresponding control (red) using an RCA assay without circular template. Even after another 90 min of reaction time, the negative control showed no hydrogel deposition, while the full RCA solution showed steady growth and about 40% hydrogel coverage at this point. Typically, in these experiments a plateau was reached after about 12 h showing 60% occupancy of the reactor area with RCA hydrogel (Figure S7a, Supporting Information). These results suggested that the RCA hydrogel formation in-flow proceeds faster than in batch experiments, where process times of 48–72 h are usually applied before the hydrogel is used for further steps.<sup>[13,14]</sup> Hence, the use of flow-driven RCA hydrogel deposition could be beneficial, for example, to generate material samples for faster evaluation of modification protocols.

As highly hydrated, highly porous materials, DNA hydrogels are ideal for the immobilization of functional proteins<sup>[15]</sup> and have already been successfully used to immobilize and increase the stability of enzymes.<sup>[16]</sup> Therefore, our hypothesis was to use the deposited DNA hydrogels as a matrix for the gentle immobilization of enzymes. This approach would have the advantage that specific Watson–Crick base pairing could be used to construct customized hybrid materials containing, for example, different enzymes with controllable stoichiometry for biocatalysis. To investigate the deposition approach for the preparation of biocatalytic DNA hybrid materials, we aimed to modify the deposited RCA material with proteins in two steps. In the first step, the formed DNA hydrogel was hybridized in the reactor with an oligonucleotide (sequence A\*, for DNA sequences, see Table S1, Supporting Information) that could specifically hybridize to the ssDNA strands of the material via complementary Watson–Crick base pairing (Figure 2e). This oligonucleotide (ST-A\*-Cy3) contained a Cy3 tag and a SpyTag (ST) modification<sup>[17]</sup> at its 3' and 5' ends, respectively, to allow fluorescence microscopy analysis and subsequent coupling of SpyCatcher (SC)-modified proteins, respectively. To ensure sufficient time in the reactor for diffusive penetration of the hydrogel matrix, the oligonucleotide solution was fed at a flow rate of  $0.1 \mu\text{L min}^{-1}$ , resulting in residence times of  $\approx 50$  s. To verify specific hybridization, a non-complementary control oligonucleotide (Control-Cy3, see Table S1, Supporting Information) was used in a parallel experiment. The fluorescence image acquired after a hybridization time of 7.5 h showed strong Cy3 fluorescence throughout the hydrogel, confirming the successful modification with the labeled oligonucleotides (Figure 2f). The time-dependent analysis showed that the reactor area covered with Cy3-labeled material increased steadily as soon as the oligonucleotide solution entered the reactor (black), reaching 30% after about 7.5 h (Figure 2g), while the control (red) showed no increase over time. The decreasing slope of surface coverage indicated that the accessible areas of the hydrogel were beginning to saturate. Experiments with longer run times showed that about 70% of the DNA hydrogel could be modified with the Cy3-oligonucleotide after 15 h (Figure S7b, Supporting Information). These results suggested that mass transport limitation occurs and hybridization is sterically hindered at denser sites of the hydrogel. Since no fluorescence increase was observed in the control experiments with the non-complementary oligonucleotide, the experiments clearly showed that the change was due exclusively to specific Watson–Crick base pairing.

In a second modification step, SC-modified enhanced green fluorescent protein (SC-eGFP) was now to be bound to the

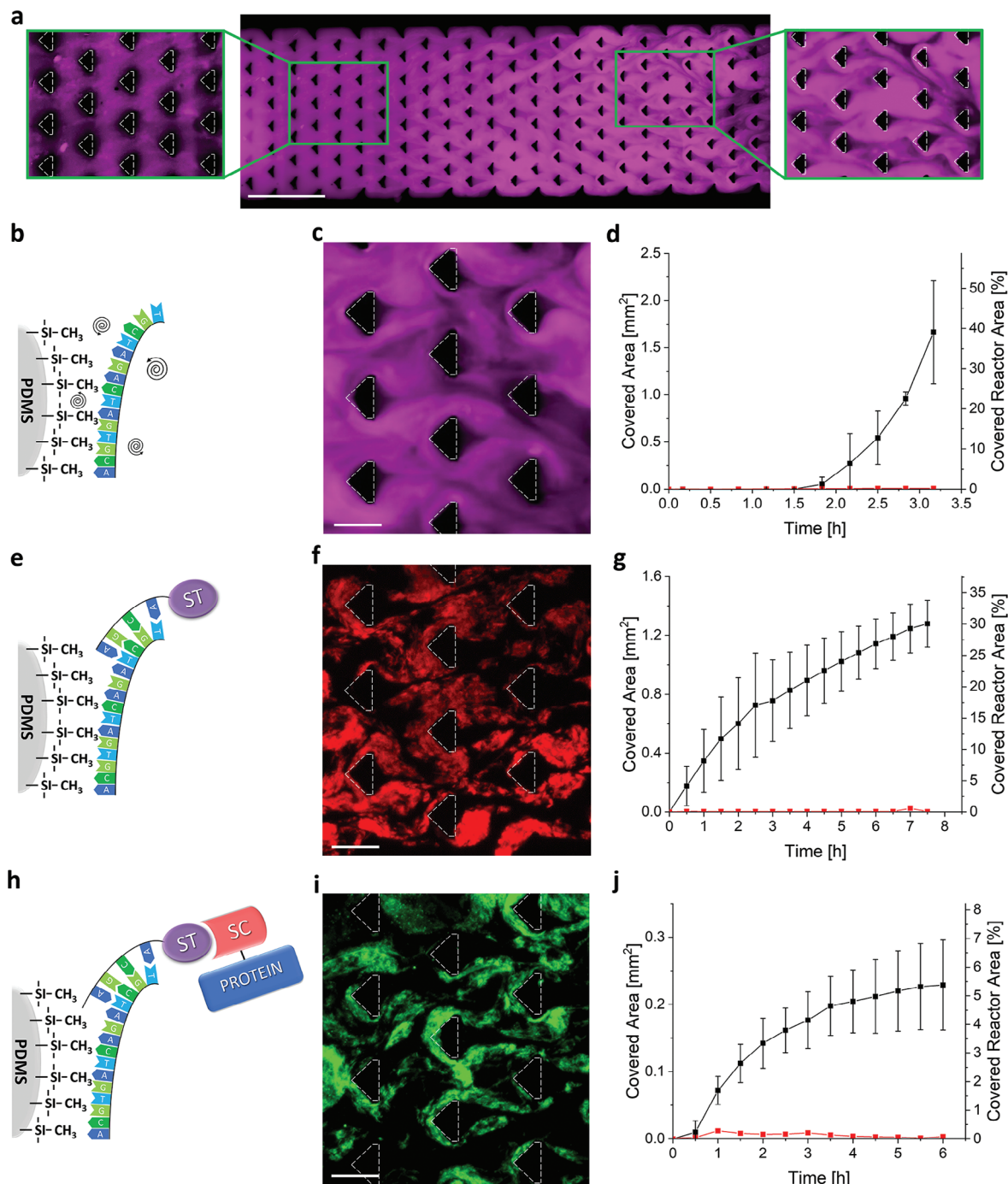


**Figure 2.** Flow-induced deposition and modification of DNA materials. a) Deposition of a DNA hydrogel at a flow rate of  $1 \mu\text{L min}^{-1}$  after 9 h. Both the front (left) and the rear (right) part of the reactor are shown enlarged. Scale bar: 500  $\mu\text{m}$ . b–j) Deposition and sequential modification of a DNA hydrogel. The black and red data points in the graphs represent the assays and negative controls, respectively. b) Schematics of the physisorption of ssDNA of the RCA product to the hydrophobic PDMS under the harsh flow conditions (indicated by the vortices). c) The fluorescence image shows the flow-based deposition of Cy5-labeled DNA material forming a hydrogel deposited at the pillars. d) Time-dependent coverage of the reactor area determined by image analysis based on Cy5 fluorescence microscopy measurements. Note the steep increase after 1.8 h, whereas the negative control (RCA mixture lacking the circular template) showed no increase in fluorescence signal. e, f) Schematic (e) and microscopic (f) depiction of the modification of the immobilized DNA material with a complementary Cy3- and SpyTag (ST)-labeled oligonucleotide, visualized by using Cy3 emission channel. g) Time-dependent evolution of reactor area coverage with Cy3-labeled material. Note that the control with a non-complementary oligonucleotide shows no increase in fluorescence over time. h, i) Schematic (h) and microscopic (i) illustration of the modification of the immobilized ST-modified DNA material with SpyCatcher (SC)-tagged green fluorescent protein (SC-eGFP, visible in the green channel). j) Time-dependent increase of eGFP fluorescence in the material-covered reactor area. Note the steady increase in the initial phase and the subsequent saturation of the material deposition. Scale bars in (b), (d), and (f): 100  $\mu\text{m}$ .

ST-functionalized DNA hydrogel (Figure 2h). For this purpose, SC-eGFP was passed through the reactor at a flow rate of  $0.1 \mu\text{L min}^{-1}$  and the immobilized protein was detected by eGFP fluorescence. Although the intense fluorescence signals observable after 6 h of flow-through time (Figure 2i) did not allow endpoint analysis of individual images due to the overlapping fluorescence of eGFP and Cy3,<sup>[18]</sup> time-resolved evaluation by segmentation image analysis (Figure S6, Supporting Information) allowed us to quantify the increase in eGFP fluorescence over time and to demonstrate successful binding of SC-eGFP to the hydrogel (Figure 2j). After 6 h, saturation was reached at only about 5.5% of the covered reactor area (black). Since no fluorescence increase was observed in the control (red) with ST-labeled eGFP, which cannot bind to ST-labeled DNA hydrogel, these results clearly indicated that the modification was due to ST/SC coupling. Further studies showed for a DNA hydrogel that had been 70% functionalized with ST-oligonucleotide by long reaction times that even at this high density of ST binding sites, only up to 9% of the DNA hydrogel could be loaded with SC-eGFP (Figure S7c, Supporting Information). The results obtained for functionalization of the DNA hydrogel with ST-oligonucleotide and SC-eGFP consistently indicate mass transport limitation and steric restriction of diffusion of bulky molecules through the DNA hydrogel matrix. Since SC-eGFP (40.2 kDa) has a much larger steric requirement than the slender ST-oligonucleotide, these effects are much more pronounced for the protein.

Even though the coupling of (strept)avidin to biotinylated DNA hydrogels has already been presented in the earlier work on flow-induced deposition in microstructures,<sup>[9]</sup> the results obtained here go beyond this, as for the first time a protein-based coupling system could be employed in this approach, based on the widely used SC/ST technology.<sup>[19]</sup> However, because the low immobilization rates observed here with the relatively small protein eGFP were not promising for efficient immobilization of larger, bulkier enzymes that often have molecular weights of larger 100 kDa. Therefore, the use of such DNA–protein hybrid materials in the reactor did not seem promising for applications in biocatalysis, and we instead focused on direct deposition of functional enzymes.

### 2.3. Flow-Induced Deposition of Protein Materials

Since the deposition and modification of DNA materials using flow energy had proven remarkably efficient, we now wanted to investigate this approach for the direct flow-induced deposition of protein materials. This seemed particularly promising with respect to self-assembling protein systems, since, for example, ST/SC-based assembly of enzymes can generate macroscopic protein structures that form a hydrogel similar to DNA materials and have shown high performance as so-called all-enzyme hydrogels (AEHs) for biocatalytic continuous flow processes.<sup>[20]</sup> To this end, the feasibility of microfluidic protein deposition was first examined using a model system of bovine serum albumin (BSA) and the protein crosslinking reagent glutaraldehyde. We first used a rhombic reactor, different from the reactor shown in Figure 1, whose widening and narrowing shape allowed us to study multiple flow velocities in the reactor at a single ap-

plied flow rate. The flow velocities within the reactor resulting from the flow rate used were previously determined by simulations (Figure S8, Supporting Information). Experimental evaluation revealed that deposition of cross-linked BSA was efficient in a protein concentration range of  $0.01\text{--}100 \mu\text{M}$  at a flow rate of  $4 \mu\text{L min}^{-1}$ , while no deposition was detectable at  $0.4 \mu\text{L min}^{-1}$  at a concentration of  $5 \mu\text{M}$  or lower, even after 65 h of perfusion (Figure S9, Supporting Information).

Since flow-induced immobilization of the model system was successful, the immobilization of SC/ST-modified variants of the enzyme phenolic acid decarboxylase (EsPAD) was next investigated. For this purpose, an SC-EsPAD and an EsPAD-ST<sub>2</sub> variant were used in a 2:1 ratio, which can self-assemble into AEH networks due to their dimeric quaternary structure.<sup>[21]</sup> Since a high concentration of ST/SC-labeled enzymes of  $500 \mu\text{M}$  or more is required for the formation of AEH under batch conditions,<sup>[20–22]</sup> it should be investigated on the basis of the above results whether AEH formation under flow conditions is also possible with lower protein concentrations. Therefore, the studies were typically performed with a total EsPAD concentration of  $4 \mu\text{M}$  (SC/2xST ratio 2:1), supplemented with  $0.15 \mu\text{M}$  eGFP-ST<sub>2</sub> to allow continuous monitoring of the process by fluorescence microscopy, at a flow rate of  $4 \mu\text{L min}^{-1}$ . Figure 3a shows the characteristic course of protein deposition as well as fluorescence images from selected time points of the deposition experiment. After about 5–6 h, a significant area of the reactor was covered with protein material and the further increase progressed into saturation. Evaluation by segmentation image analysis showed that after 10 h, about 20% of the surface was covered with protein materials, with the reactor still showing good transfusion and no signs of clogging. Of note, the comparison of the experimental data of protein deposition at the pillars of the reactor with the flow simulations (Figure S10, Supporting Information) also revealed that the flow-induced immobilization of the protein takes place at the lateral edges of the pillars, where high vorticity and shear rates prevail. In contrast, no significant protein deposition was observed in the dead zone (very low vorticity, shear rates and flow velocity) behind the columns.

To further characterize the dynamics of SC/ST-EsPAD deposition, the process parameters were investigated with respect to systematically at different flow rates (1, 2, and  $4 \mu\text{L min}^{-1}$ ) at constant protein concentration ( $4 \mu\text{M}$ ) and different protein concentrations (1, 2, and  $4 \mu\text{M}$ ) at constant flow rate ( $4 \mu\text{L min}^{-1}$ ) (Figures 3b,c, respectively). We found that the amount of deposited material increased with increasing flow rate. While essentially no protein deposition (<0.5%) was observed at  $1 \mu\text{L min}^{-1}$  even after 10 h,  $\approx 7\%$  of the reactor area was occupied at this time at  $2 \mu\text{L min}^{-1}$  and  $\approx 24\%$  at  $4 \mu\text{L min}^{-1}$ . This supports the assumption that flow energy in the form of shear stress and vorticity is a critical factor for material deposition.<sup>[23]</sup> The dependence of material deposition on concentration of protein used shows a similar pattern. Compared to about 24% of the material deposited at  $4 \mu\text{M}$ , only about 9% and 4% of the material was deposited at 2 and  $1 \mu\text{M}$ , respectively. Thus, protein concentration is another critical factor, which was consistent with the expectation that greater collision probabilities and thus enhanced flow-induced precipitation of molecules can occur at higher concentrations.

The EsPAD variants used had been selected because they can form cross-linked AEH through the SC-ST interaction.<sup>[21]</sup>

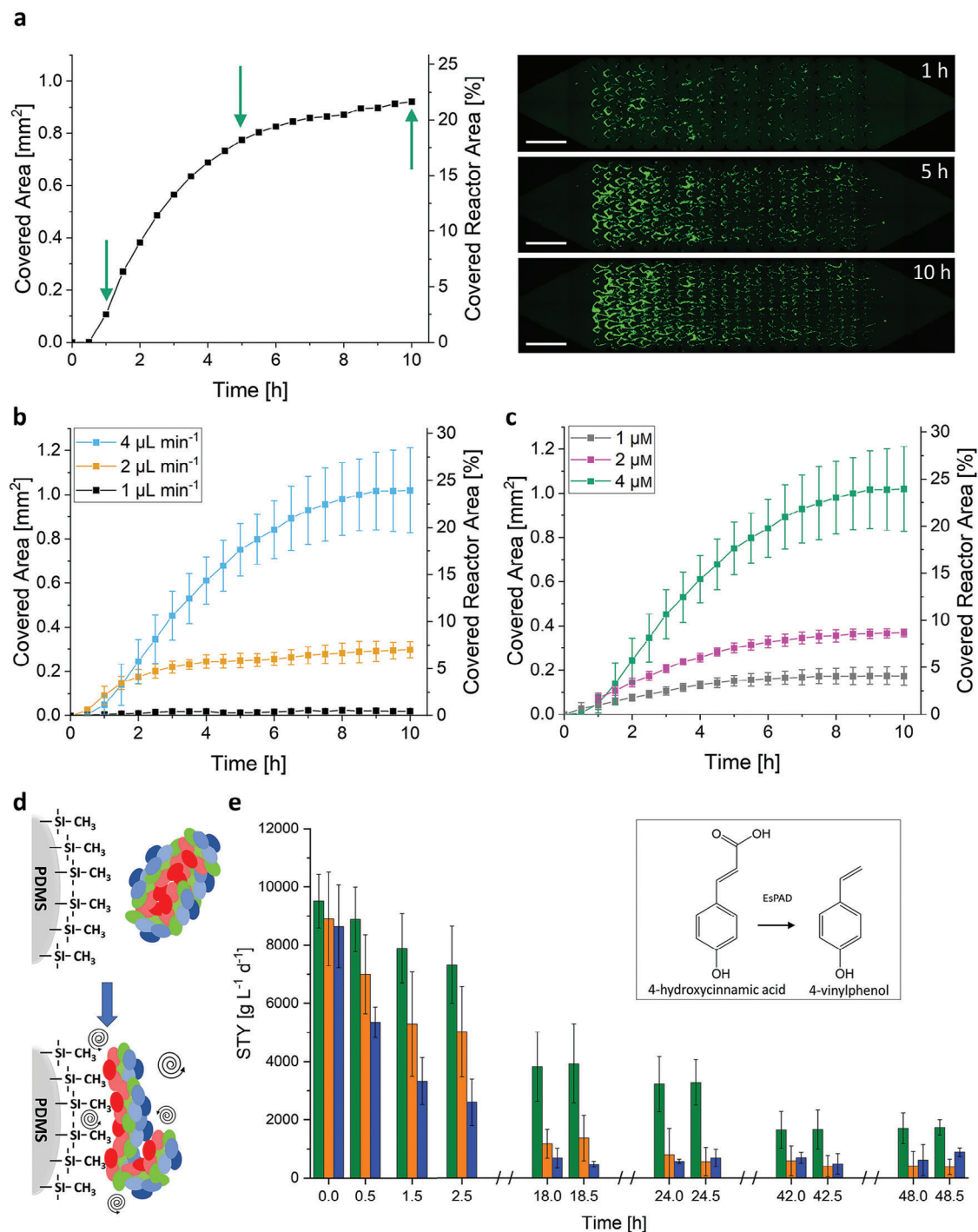


**Figure 3.** Flow-induced immobilization of protein materials. a) Representative deposition of phenolic acid decarboxylase (EsPAD;  $4 \mu\text{M}$ ) doped with green fluorescent protein (eGFP;  $0.15 \mu\text{M}$ ) at a flow rate of  $4 \mu\text{L min}^{-1}$ . The graph depicts the time-resolved deposition process analyzed by software-assisted evaluation of continuously acquired fluorescence images. Shown is the area of protein coverage over time the reactor is continuously perfused with protein solution. The arrows indicate the different time points shown in the fluorescence images on the right. Scale bars:  $500 \mu\text{m}$ . b) Time-dependent evolution of the reactor area covered with protein material in the deposition process at different flow rates at a constant protein concentration of  $4 \mu\text{M}$  EsPAD and  $0.15 \mu\text{M}$  eGFP. c) Time-dependent evolution of reactor area coverage with protein material at different EsPAD concentrations ( $1, 2,$  and  $4 \mu\text{M}$  supplemented with  $0.15 \mu\text{M}$  eGFP) at identical flow rate of  $4 \mu\text{L min}^{-1}$ . d) Flow-induced deposition of proteins. Due to the harsh flow conditions (indicated by the vortices) at the pillars of the reactor, the proteins (partially) unfold, exposing the inner hydrophobic regions (red) of the protein and allowing them to physisorb to the hydrophobic PDMS. e) Space-time yields (STY) of flow-deposition reactors with immobilized EsPAD in different variations, determined by the conversion of 4-hydroxycinnamic acid (HCA) to 4-vinylphenol (VP). The green bars represent a reactor containing preformed EsPAD-ST<sub>2</sub> scaffold that was subsequently functionalized with SC-EsPAD, the orange bars represent an EsPAD-ST<sub>2</sub> scaffold without additional SC-EsPAD, perfusion, and the blue bars represent a reactor that does not contain a scaffold structure but was perfused with SC-EsPAD.

Surprisingly, however, control experiments using only one variant labeled with SC or ST at a time also showed an almost equal tendency for flow-induced deposition (Figure S11a,b, Supporting Information). Therefore, SC-ST coupling did not seem to affect the flow-based deposition process, so that there was no entanglement of protein chains as assumed for DNA hydrogels, but primarily denaturation of proteins by shear forces with subsequent adsorption of these molecules due to their increasing hydrophobicity takes place as already observed for VWF and other proteins<sup>[24]</sup> (see schematics in Figure 3d). Indeed, the deposited protein material clearly showed dark structures with reduced light transmission in brightfield images, which is characteristic of precipitated denatured proteins (Figure S11c,d, Supporting Information).<sup>[25]</sup> Furthermore, we investigated the deposition of other established enzymes, such as the two-enzyme system consisting of an alcohol dehydrogenase and a glucose dehydrogenase (Figure S12, Supporting Information).<sup>[20]</sup> These studies indeed showed a comparable pattern of protein deposition, albeit with a slightly lower overall occupancy of the reactor. Subsequent activity studies revealed that the deposited protein material had very low enzyme activity, which was taken as a clear indication of denaturation. We note that it would be very interesting and should be possible in subsequent studies to correlate the experimentally determinable deposition rates with a quantitative assessment of tertiary structure stability, for example, by using computational modeling of the various proteins used here.

Since enzymes lose their catalytic activity upon denaturation, an alternative process had to be used to generate a biocatalytically active chip device by flow-induced deposition. Therefore, in a first step, we aimed to deposit ST-labeled enzyme under denaturing conditions at a high flow rate ( $4 \mu\text{L min}^{-1}$ ) in the reactor and then use the resulting protein structure as an “ST-scaffold” to attach functional SC-EsPAD at a low flow rate ( $0.04 \mu\text{L min}^{-1}$ ) under non-denaturing conditions in a second step. This two-step protein immobilization process was performed with EsPAD in order to investigate the catalytic performance of the reactor unit (Figure 3e). Here, it was first of interest to understand whether the ST-scaffold deposited by the harsh flow conditions still possessed catalytic activity and whether the ST domains of the scaffold retained their ability to bind SC-EsPAD.

Since proteins can adsorb non-specifically to the reactor surface due to the hydrophobicity of PDMS,<sup>[26]</sup> control experiments (blue bars, in Figure 3e) were first performed in which EsPAD-ST<sub>2</sub> was applied at a low flow rate ( $0.04 \mu\text{L min}^{-1}$ ) so that no fiber-like structures were visible and thus no ST-scaffold was formed. Consequently, any proteins were immobilized only due to physisorption on the surface of the reactor. In the second step, SC-EsPAD was pumped through the reactor at a flow rate of  $0.004 \mu\text{L min}^{-1}$  to achieve binding with the adsorbed ST-tagged protein. This corresponded to a residence time in the reactor of  $\approx 20$  min, which should be sufficient for the reaction of the SC/ST system.<sup>[27]</sup> To analyze the catalytic activity, the conversion of 4-hydroxycinnamic acid (HCA) to 4-vinylphenol (VP) catalyzed by EsPAD was carried out at a flow rate of  $1 \mu\text{L min}^{-1}$ , the product concentration was determined by HPLC analysis,<sup>[28]</sup> and the space-time yield (STY) was calculated for different time points (Figure 3e, blue bars). The data showed that the reactor containing only physisorbed EsPAD had relatively high activity at the be-

ginning of catalysis, but it decreased sharply after the first 2.5 h, and after 18 h it was only 8% of the initial STY. This finding suggested that the enzymes immobilized by adsorption were washed out of the reactor relatively quickly during the continuous reaction processes.

In further control experiments (orange bars, in Figure 3e), the (residual) catalytic activity of the ST-scaffold was measured, which in a first step was deposited at  $4 \mu\text{L min}^{-1}$  with EsPAD-ST<sub>2</sub>, and in a second step was overflushed only with pure sodium phosphate buffer instead of SC-EsPAD at a flow rate of  $0.004 \mu\text{L min}^{-1}$ . At the beginning of the biocatalysis process, performed at  $1 \mu\text{L min}^{-1}$  flow rate, a decrease in STY was also observed in these experiments within the first 2.5 h, but it was much less pronounced compared to the experiments without ST-scaffold (blue). These results indicated that due to the deposited ST-scaffold, larger amounts of enzymes were present in the reactor than in the case of the surface adsorbed enzymes and that the ST-scaffold has significant residual catalytic activity. It appeared that active protein was washed out of the reactor during the process, so that after reaction times  $>18$  h, the STY showed virtually no difference from the reactor without ST-scaffold structure (blue). The comparison of brightfield microscopy images before and after 28 h of catalysis did not provide any indication of substantial leaching of the immobilized material from the flow reactor (Figure S13, Supporting Information). In contrast, fluorescence microscopy images showed a decrease in the fluorescence signal over the observation period, which roughly correlated with the decrease in the catalytic performance of the enzyme materials (Figure S13, Supporting Information). However, since the decreasing GFP fluorescence only gives an indirect indication of the presence and integrity of the enzymes and may also be due to photobleaching, we assume that a weak leaching of loosely bound material takes place.

To investigate whether the two-stage immobilization described above leads to improved catalytic performance of the reactor, the ST-scaffold was first generated at a high flow rate and then functionalized with SC-EsPAD at a low flow rate (green bars, in Figure 3e). Indeed, the progression of STY values showed a much smaller decrease over time and thus a more constant catalytic performance compared to the control experiments (blue, orange). Specifically, STY decreased from  $9514 \text{ g L}^{-1} \text{ d}^{-1}$  at the beginning of catalysis to  $7330 \text{ g L}^{-1} \text{ d}^{-1}$  after 2.5 h, which corresponded to a 2.8-fold increase compared to the experiments without scaffold structure (blue) or a 1.5-fold increase compared to the experiments with scaffold but lacking the SC counterpart (orange). After 24 h, about 34% of the initial activity was still observed, while the two controls were at about 8% residual activity. This demonstrated that two-stage immobilization can still achieve considerable reactor performance with an STY of  $3227 \text{ g L}^{-1} \text{ d}^{-1}$ , even for longer catalysis processes. Published comparative data obtained with this enzyme system in a conventional microreactor channel gave STY values of  $57.7 \text{ g L}^{-1} \text{ d}^{-1}$  over 10 h.<sup>[21]</sup> This  $\approx 50$ -fold higher reactor performance obtained here suggests that the deposition reactor could in principle be developed into a very powerful device for biocatalysis. However, it should be noted that the short residence time and mechanical stability of the proteins are limiting factors for this reactor system, which must be counteracted by careful selection of the enzymes to be immobilized.

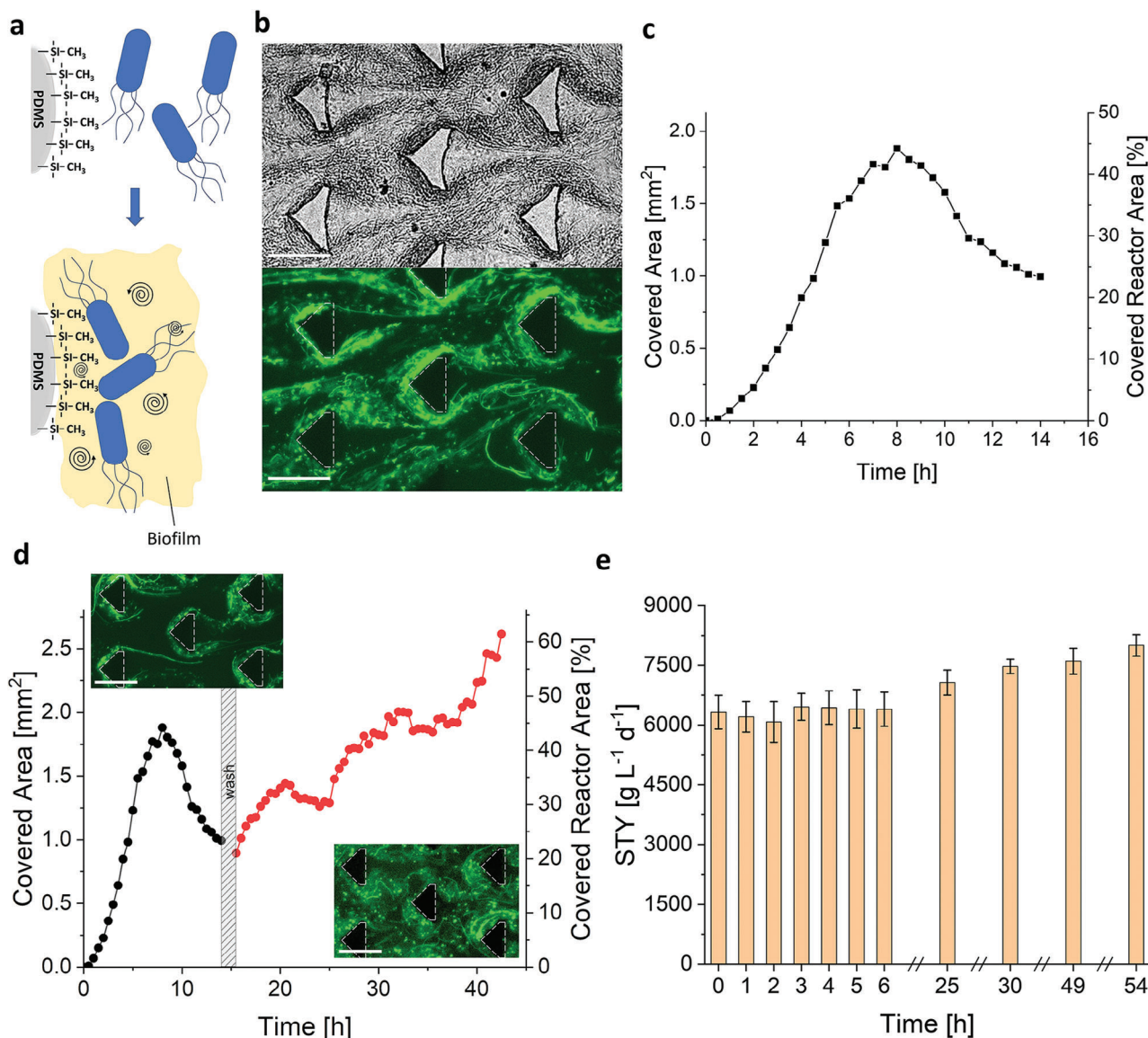


**Figure 4.** Flow-induced immobilization of *E. coli* cells inside the microfluidic pillar reactor. a) Schematic representation of the flow-induced deposition of biofilm-forming whole cells mediated by the harsh flow conditions (indicated by the vortices). b) Detail images of deposited material from *E. coli* bacteria expressing eGFP, obtained at  $4 \mu\text{L min}^{-1}$ . Shown is a brightfield (top) and a fluorescence image (bottom), which also shows the characteristic green fluorescent bacterial filaments. c) Cell covered area of the reactor over process time determined by image analysis ( $4 \mu\text{L min}^{-1}$ , initial OD: 0.05). d) Two-step cell immobilization, shown as the covered reactor area as a function of process time. In the first step (black), cell deposition was performed with a cell suspension (initial optical density (OD): 0.05) at a flow rate of  $4 \mu\text{L min}^{-1}$ . After brief washing with fresh medium at  $4 \mu\text{L min}^{-1}$ , the flow rate was decreased to  $0.1 \mu\text{L min}^{-1}$  (red) and cell growth was monitored in the reactor under continuous perfusion with fresh medium. e) STY of immobilized *E. coli* cell material expressing EsPAD. Catalysis of HCA to VP was achieved at a constant flow rate of  $1 \mu\text{L min}^{-1}$ . Scale bars:  $100 \mu\text{m}$ .

#### 2.4. Flow-Induced Deposition of Whole-Cell Biocatalysts

The above studies on shear-induced deposition of enzyme materials showed that while the reactor system can provide significant benefits as a catalytic unit, the stability of the catalysts is a limiting factor for applications in biocatalysis. To address this issue, we wanted to investigate whether whole cells could be immobilized in the reactor, in order to use the resulting device for whole-cell biocatalysis, in which catalytically active enzymes are expressed directly in the cell and thus protected from flow forces

in the reactor. It is known that bacterial cells respond to flow forces and that high shear forces can trigger strong cell aggregation and biofilm formation,<sup>[29]</sup> which involves the formation of a matrix called extracellular polymeric substance (EPS) in which the cells are embedded and which supports further cell adhesion. Therefore, we assumed a biofilm-mediated immobilization of the cells, as shown schematically in **Figure 4a**.

We first tested the whole-cell deposition process at a flow rate of  $4 \mu\text{L min}^{-1}$  using recombinant *E. coli* cells expressing eGFP. Observation of the cells by brightfield and fluorescence

microscopy (Figure 4b) clearly showed that cell deposition started at the pillars of the reactor, and by continuous deposition over time, almost half of the reactor surface was covered after about 8 h (Figure 4c). The initial deposition of cells at the pillars is likely due to adsorption on the PDMS surface in the areas of high vorticity and shear stress, similar to the deposition of the DNA and protein materials. This assumption is supported by the observation that no cell deposition was observed in the area lacking pillars at the front of the reactor (Figure S14, Supporting Information). The decrease in surface coverage observed after about 7 h (Figure 4c) could be attributed to the fact that with increasing time, cells in the reservoir outside the reactor sedimented, so that fewer new cells were flushed through the reactor, while at the same time cells were always flushed out of the reactor due to the relatively high flow rate. This observation was confirmed by independent control experiments (Figure S15, Supporting Information). Thus, the initial experiments clearly showed that the reactor can be filled with cells by flow-induced deposition. The deposited cell material was further examined by performing crystal violet (CV) staining to detect biofilm formation. The extensive, contiguous dark staining of cells and EPS in the flow-induced deposited cellular material on the columns (Figure S16, Supporting Information), which is characteristic of CV-stained biofilms,<sup>[30]</sup> supported our hypothesis of biofilm-mediated immobilization (Figure 4a).

It was subsequently examined whether the deposited cells were still viable (Figure 4d). For this purpose, after deposition of the bacteria, fresh medium was connected to the reactor and first a short wash step was performed at  $4 \mu\text{L min}^{-1}$  to remove all non-adherent cells from the system. The flow rate was then reduced to  $0.1 \mu\text{L min}^{-1}$  and cell growth was monitored for an additional 27 h. Image analysis showed that the reactor area covered by cells decreased from 23% to 21% due to the washing step. After the flow rate was reduced, a steady spread of cells was observed in the reactor, giving a clear indication of cell growth and viability. The continuous growth resulted in more than 60% occupancy of the reactor with cells, which was also clearly visible when comparing the fluorescence images directly with the naked eye (see close-up images in Figure 4d).

Based on these promising results, the aim was now to verify whether the method is also suitable for performing whole-cell biocatalysis. For this purpose, recombinant *E. coli* cells expressing EsPAD,<sup>[31]</sup> were deposited in the reactor for 15 h and the device was subsequently perfused with medium containing 5 mM of HCA at a flow rate of  $1 \mu\text{L min}^{-1}$ . During the medium change, the entire feed and waste tubing was replaced so that any cells remaining in the old tubing could not interfere with the catalysis. The conversion of HCA was quantified from the reactor effluent by HPLC analysis and the corresponding STY values were calculated (Figure 4e). The data obtained impressively showed that by using whole cells as catalyst, stable conversion could be achieved over long periods of time. While purified enzymes showed a strong decrease in catalytic efficiency already after the first few hours, constant STY values of up to  $8000 \text{ g L}^{-1} \text{ d}^{-1}$  were achieved for >50 h in the whole-cell format.

These results supported the above working hypotheses that flow-induced deposition can be used to generate a stable living material and that the cells immobilized in it form an effective protective barrier for the sensitive proteins. We also investigated

**Table 1.** Comparison of the key parameters of the deposition of different biomaterials. NA: not applicable.

Material	DNA hydrogel	Proteins (EsPAD)	Whole Cells (EsPAD)
Deposition Flow rate [ $\mu\text{L min}^{-1}$ ]	1	4	4
Deposition Temperature [ $^{\circ}\text{C}$ ]	30	30	30
Covered area after 10 h [%]	56	24	37
Catalytic stability [h]	NA	<18	>240
(>50% initial activity)			
Maximum STY [ $\text{g L}^{-1} \text{ d}^{-1}$ ]	NA	>9500 (two-step immobilization)	8001 (one-step immobilization)

the stability of the immobilized bacterial cells by depositing the recombinant EsPAD-expressing *E. coli* cells in reactors and running them continuously for 10 days (Figure S17a, Supporting Information). The experiments impressively confirmed the high robustness and performance of the cellular material. The cells even showed a regenerative capacity during an intentional starvation period of three days, during which no fresh medium was supplied to the system. Furthermore, we were not only able to demonstrate the stability and regenerative capacity of these systems in a long-term experiment, but also the transferability to other cell systems, such as recombinant *E. coli* cells overexpressing a stereoselective alcohol dehydrogenase as a catalytically active protein (Figure S17b, Supporting Information).

The comparison of various relevant key parameters such as flow rate, temperature, occupied reactor area, stability and STY to evaluate the flow-induced immobilization of different biomaterials (Table 1) clearly demonstrates the exceptional performance of the whole-cell biocatalysts with high stability and productivity. Compared to previously published data with the EsPAD enzyme system in conventional microreactors with an STY of  $57.7 \text{ g L}^{-1} \text{ d}^{-1}$ <sup>[21]</sup> and to other reactor systems such as packed bed reactors, in which the decarboxylation of HCA with PAD variants from other microorganisms was achieved with a maximum STY of  $127.7 \text{ g L}^{-1} \text{ d}^{-1}$ ,<sup>[32]</sup> the whole-cell catalysis format presented here corresponds to an about 140-fold and 60-fold increase in catalytic performance, respectively, which underlines the advanced nature of this biocatalytic material. Overall, the results obtained in this work suggest that flow-driven deposition in microreactors has great potential for new biocatalyst devices, especially when populated with living functional materials.

### 3. Conclusion

In summary, we have reported on the utilization of the energy of microfluidic flows in a specially designed microreactor for the deposition of functional materials for biocatalysis. Compared to previously described reactors,<sup>[8,9]</sup> the reactor dimensions were optimized to enable deposition of larger amounts of material and the reactor was integrated into a microfluidic operating system to allow sequential process steps, opening access to broader applications. The functionality of the new reactor device was first

confirmed using the flow-driven assembly of DNA hydrogels. The material deposited in this process was successfully converted to a biohybrid DNA–protein material in two steps by using ST/SC technology for the first time. However, since this strategy did not provide a sufficiently high immobilization rate for bulky proteins, we investigated direct deposition of the functional enzyme EsPAD. Here, we found that deposition of pure protein materials succeeded efficiently, but the benefit for biocatalysis was limited due to flow-induced denaturation of the enzyme's tertiary structure. This problem was circumvented by two-step immobilization, allowing access to microfluidic bioreactor devices that showed impressive initial performance, but whose process stability was not satisfactory. Finally, we used flow-induced material deposition to immobilize in the reactor recombinant *E. coli* cells overexpressing biocatalytically relevant enzymes. This method has been very successful and offers a viable, efficient and broadly applicable approach for microfluidic reactors that exhibit very high STYs in living whole-cell catalysis continuously over several days.

The lessons learned here open the door for further optimization of this innovative reactor system to maximize the benefits shown and implement them for applications. Importantly, an up-scaling of our strategy would be possible. The starting material, recombinant *E. coli* cells, can easily be produced in large quantities by conventional liquid phase cultivation, and our microfluidic systems could be upscaled via the so-called numbering-up strategy by using efficient manufacturing processes such as hot-stamping, roll-to-roll, or injection molding. An exemplary model estimate based on a given STY of  $8000 \text{ g L}^{-1} \text{ d}^{-1}$  and a flow rate of  $1 \mu\text{L min}^{-1}$  suggests that only about 90 of the bioreactors described here would be needed to produce 1 kg of substrate per day. In addition to direct applications for biocatalytic production of valuable molecules or, in bioremediations, the degradation of contaminants, we believe that the study presented here also provides concrete starting points to advance the booming field of engineered living materials.<sup>[33]</sup> Therefore, this study supplements and underscores the significance of inventive approaches in creating efficient biocatalyst devices. These methods are currently in progress for both isolated enzymes and related material systems,<sup>[34]</sup> aiming to enhance research and development across various domains in life sciences and materials science.

## Supporting Information

Supporting Information is available from the Wiley Online Library or from the author.

## Acknowledgements

This work was financially supported through the Helmholtz Association program “Materials Systems Engineering” under the topic “Adaptive and Bioinstructive Materials Systems” and by the German government, through BMBF projects MicroMatrix (project ID: 161L0284A) and Multi-pore (project ID: 13FH020KX0).

Open access funding enabled and organized by Projekt DEAL.

## Conflict of Interest

The authors declare no conflict of interest.

## Data Availability Statement

The data that support the findings of this study are available from the corresponding author upon reasonable request.

## Keywords

biocatalysis, biomaterials, flow-catalysis, microfluidics, microreactor

Received: November 7, 2023

Revised: January 10, 2024

Published online:

- a) S. F. D'Souza, *Biotechnol. Appl. Biochem.* **2001**, *96*, 225; b) R. A. Sheldon, S. van Pelt, *Chem. Soc. Rev.* **2013**, *42*, 6223; c) D. Kim, A. E. Herr, *Biomicrofluidics* **2013**, *7*, 041501; d) N. Adebear, A. Nastke, H. Gröger, *React. Chem. Eng.* **2021**, *6*, 977.
- M. L. Salva, M. Rocca, C. M. Niemeyer, E. Delamarche, *Micro Nano Eng.* **2021**, *11*, 100085.
- a) A. Kuchler, M. Yoshimoto, S. Luginbuhl, F. Mavelli, P. Walde, *Nat. Nanotechnol.* **2016**, *11*, 409; b) S. P. France, L. J. Hepworth, N. J. Turner, S. L. Flitsch, *ACS Catal.* **2017**, *7*, 710; c) K. S. Rabe, J. Muller, M. Skoupi, C. M. Niemeyer, *Angew Chem Int Ed Engl.* **2017**, *56*, 13574; d) J. Britton, S. Majumdar, G. A. Weiss, *Chem. Soc. Rev.* **2018**, *47*, 5891; e) L. L. Martin, T. Peschke, F. Venturoni, S. Mostarda, *Curr Opin Green Sustain Chem.* **2020**, *25*, 100350.
- S. F. D'Souza, *Biosens. Bioelectron.* **2001**, *16*, 337.
- O. J. G. M. Goor, S. I. S. Hendrikse, P. Y. W. Dankers, E. W. Meijer, *Chem. Soc. Rev.* **2017**, *46*, 6621.
- A. Sorrenti, J. Leira-Iglesias, A. J. Markvoort, T. F. A. de Greef, T. M. Hermans, *Chem. Soc. Rev.* **2017**, *46*, 5476.
- B. A. Grzybowski, W. T. S. Huck, *Nat. Nanotechnol.* **2016**, *11*, 585.
- Y. Zheng, J. Chen, J. A. López, *Nat Commun.* **2015**, *6*, 7858.
- S. Hamada, K. G. Yancey, Y. Pardo, M. Gan, M. Vanatta, D. An, Y. Hu, T. L. Derrien, R. Ruiz, P. Liu, J. Sabin, D. Luo, *Sci Robot.* **2019**, *4*, eaaw3512.
- J. E. Sadler, *Annu. Rev. Med.* **2004**, *56*, 173.
- T. Toftberg, M. Skolimowski, E. Andreassen, O. Geschke, *Microfluid Nanofluidics* **2010**, *8*, 209.
- a) M. Soos, A. S. Moussa, L. Ehrl, J. Sefcik, H. Wu, M. Morbidelli, *J. Colloid Interface Sci.* **2008**, *319*, 577; b) A. Campesi, M. O. Cerri, C. O. Hokka, A. C. Badino, *Bioprocess Biosyst. Eng.* **2009**, *32*, 241; c) H. Wang, X. Duan, X. Feng, Z.-S. Mao, C. Yang, *Chin. J. Chem. Eng.* **2022**, *42*, 351.
- R. Merindol, G. Delechiave, L. Heinen, L. H. Catalani, A. Walther, *Nat. Commun.* **2019**, *10*, 528.
- a) Y. Huang, W. Xu, G. Liu, L. Tian, *Chem. Commun.* **2017**, *53*, 3038; b) Y. Hu, C. M. Domínguez, J. Bauer, S. Weigel, A. Schipperges, C. Oelschlaeger, N. Willenbacher, S. Keppler, M. Bastmeyer, S. Heißler, C. Wöll, T. Scharnweber, K. S. Rabe, C. M. Niemeyer, *Nat. Commun.* **2019**, *10*, 5522; c) L. Schneider, M. Richter, C. Oelschlaeger, K. S. Rabe, C. M. Domínguez, C. M. Niemeyer, *Chem. Commun.* **2023**, *59*, 12184.
- Y. Hu, C. M. Niemeyer, *Adv. Mater.* **2019**, *31*, 1806294.
- a) K. Van Nguyen, S. D. Minter, *Chem. Commun.* **2015**, *51*, 13071; b) L. Wan, Q. Chen, J. Liu, X. Yang, J. Huang, L. Li, X. Guo, J. Zhang, K. Wang, *Biomacromolecules* **2016**, *17*, 1543.
- S. Kröll, L. Schneider, P. Wadhvani, K. S. Rabe, C. M. Niemeyer, *Chem. Commun.* **2022**, *58*, 13471.
- T. Aoyama, A. Kato, E. Nishimoto, *J. Fluoresc.* **2020**, *30*, 1121.
- A. H. Keeble, M. Howarth, *Chem. Sci.* **2020**, *11*, 7281.

- [20] T. Peschke, P. Bitterwolf, S. Gallus, Y. Hu, C. Oelschlaeger, N. Willenbacher, K. S. Rabe, C. M. Niemeyer, *Angew Chem Int Ed Engl.* **2018**, *57*, 17028.
- [21] E. Mittmann, S. Gallus, P. Bitterwolf, C. Oelschlaeger, N. Willenbacher, C. M. Niemeyer, K. S. Rabe, *Micromachines* **2019**, *10*, 795.
- [22] a) P. Bitterwolf, S. Gallus, T. Peschke, E. Mittmann, C. Oelschlaeger, N. Willenbacher, K. S. Rabe, C. M. Niemeyer, *Chem. Sci.* **2019**, *10*, 9752; b) T. Peschke, P. Bitterwolf, K. S. Rabe, C. M. Niemeyer, *Chem. Eng. Technol.* **2019**, *42*, 2009.
- [23] J. D. Debus, M. Mendoza, S. Succi, H. J. Herrmann, *Sci. Rep.* **2017**, *7*, 42350.
- [24] a) S. W. Schneider, S. Nuschele, A. Wixforth, C. Gorzelanny, A. Alexander-Katz, R. R. Netz, M. F. Schneider, *Proc. Nat. Acad. Sci. U. S. A.* **2007**, *104*, 7899; b) J. Dobson, A. Kumar, L. F. Willis, R. Tuma, D. R. Higazi, R. Turner, D. C. Lowe, A. E. Ashcroft, S. E. Radford, N. Kapur, D. J. Brockwell, *Proc. Nat. Acad. Sci. U. S. A.* **2017**, *114*, 4673.
- [25] a) B. Demeule, R. Gurny, T. Arvinte, *Int. J. Pharm.* **2007**, *329*, 37; b) F. J. Galindo-Rosales, *Appl. Sci.* **2016**, *6*, 206.
- [26] D. Bodas, C. Khan-Malek, *Sens. Actuators, B.* **2007**, *123*, 368.
- [27] B. Zakeri, J. O. Fierer, E. Celik, E. C. Chittock, U. Schwarz-Linek, V. T. Moy, M. Howarth, *Proc Natl Acad Sci USA* **2012**, *109*, E690.
- [28] E. Mittmann, F. Mickoleit, D. S. Maier, S. Y. Stäbler, M. A. Klein, C. M. Niemeyer, K. S. Rabe, D. Schüler, *ACS Appl. Mater. Interfaces* **2022**, *14*, 22138.
- [29] A. Park, H.-H. Jeong, J. Lee, K. P. Kim, C.-S. Lee, *BioChip J.* **2011**, *5*, 236.
- [30] a) S. Qayyum, M. Oves, A. U. Khan, *PLoS One* **2017**, *12*, 0181363; b) A. E. Zoheir, G. P. Späth, C. M. Niemeyer, K. S. Rabe, *Small* **2021**, *17*, 2007166.
- [31] P. Lemke, A. E. Zoheir, K. S. Rabe, C. M. Niemeyer, *Biotechnol. Bioengin.* **2021**, *118*, 3860.
- [32] a) D.-H. Jung, W. Choi, K.-Y. Choi, E. Jung, H. Yun, R. J. Kazlauskas, B.-G. Kim, *Appl. Microbiol. Biotechnol.* **2013**, *97*, 1501; b) B. Grabner, A. K. Schweiger, K. Gavric, R. Kourist, H. Gruber-Woelfler, *React. Chem. Eng.* **2020**, *5*, 263.
- [33] a) P. Q. Nguyen, N.-M. D. Courchesne, A. Duraj-Thatte, P. Praveschotununt, N. S. Joshi, *Adv. Mater.* **2018**, *30*, 1704847; b) G. Altin-Yavuzarslan, S. M. Brooks, S. F. Yuan, J. O. Park, H. S. Alper, A. Nelson, *Adv. Funct. Mater.* **2023**, *33*, 2300332.
- [34] a) H. Xia, N. Li, W. Huang, Y. Song, Y. Jiang, *ACS Appl. Mater. Interfaces* **2021**, *13*, 22240; b) R. Greifenstein, T. Ballweg, T. Hashem, E. Gottwald, D. Achauer, F. Kirschhöfer, M. Nusser, G. Brenner-Weiß, E. Sedghamiz, W. Wenzel, E. Mittmann, K. S. Rabe, C. M. Niemeyer, M. Franzreb, C. Wöll, *Angew Chem Int Ed Engl.* **2022**, *61*, 202117144; c) W. Liang, P. Wied, F. Carraro, C. J. Sumbly, B. Nidetzky, C.-K. Tsung, P. Falcaro, C. J. Doonan, *Chem. Rev.* **2021**, *121*, 1077; d) D. Tian, X. Zhang, H. Shi, L. Liang, N. Xue, J.-H. Wang, H. Yang, *J. Am. Chem. Soc.* **2021**, *143*, 16641; e) Q. Chen, G. Qu, X. Li, M. Feng, F. Yang, Y. Li, J. Li, F. Tong, S. Song, Y. Wang, Z. Sun, G. Luo, *Nat. Commun.* **2023**, *14*, 2117; f) Q. Chen, Y. An, M. Feng, J. Li, Y. Li, F. Tong, G. Qu, Z. Sun, Y. Wang, G. Luo, *Green Chem.* **2022**, *24*, 9508; g) R. Hao, M. Zhang, D. Tian, F. Lei, Z. Qin, T. Wu, H. Yang, *J. Am. Chem. Soc.* **2023**, *145*, 20319; h) J. S. Hertel, P. Bitterwolf, S. Kröll, A. Winterhalter, A. J. Weber, M. Grösche, L. B. Walkowsky, S. Heißler, M. Schwotzer, C. Wöll, T. van de Kamp, M. Zuber, T. Baumbach, K. S. Rabe, C. M. Niemeyer, *Adv. Mater.* **2023**, *35*, 2303952; i) S. Kröll, C. M. Niemeyer, *Angew Chem Int Ed Engl.* **2023**, *63*, 202314452.